

Article

Monitoring of Thermoacoustic Combustion Instability via Recurrence Quantification Analysis and Optimized Deep Belief Network

Qingwen Zeng ^{1,2,3}, Chunyan Hu ^{1,2,3,*}, Jiaxian Sun ^{1,3}, Yafeng Shen ^{1,3} and Keqiang Miao ^{1,3}

¹ Key Laboratory of Light-Duty Gas-Turbine, Institute of Engineering Thermophysics, Chinese Academy of Sciences, Beijing 100190, China; zengqingwen@iet.cn (Q.Z.); sunjiaxian@iet.cn (J.S.); shenyafeng@iet.cn (Y.S.); miaokeqiang@iet.cn (K.M.)

² University of Chinese Academy of Sciences, Beijing 100049, China

³ National Key Laboratory of Science and Technology on Advanced Light-Duty Gas-Turbine, Beijing 100190, China

* Correspondence: huchunyan@iet.cn

Abstract: Thermoacoustic oscillation is indeed a phenomenon characterized by the symmetric coupling of thermal and acoustic waves. This paper introduces a novel approach for monitoring and predicting thermoacoustic combustion instability using a combination of recurrence quantification analysis (RQA) and an optimized deep belief network (DBN). Six samples of combustion state data were collected using two distinct types of burners to facilitate the training and validation of GA-DBN. The proposed methodology leverages RQA to extract intricate patterns and dynamic features from time series data representing combustion behavior. By quantifying the recurrence plot of specific patterns, the analysis provides valuable insights into the underlying thermoacoustic dynamics. Among three different feature extraction methods, RQA stands out remarkably in performance. These RQA-derived features serve as input to a carefully tuned DBN, which is trained to learn the complex relationships within the combustion process. The classification accuracy of deep belief network optimized by genetic algorithm (GA-DBN) reached an impressive 99.8%. Subsequent multiple comparisons were conducted between GA-DBN, DBN, and support vector machine (SVM), revealing that GA-DBN consistently demonstrated satisfactory classification results. This method holds significant importance in monitoring intricate combustion states.

Keywords: thermoacoustic instability; recurrence quantification analysis; optimized deep belief network



Citation: Zeng, Q.; Hu, C.; Sun, J.; Shen, Y.; Miao, K. Monitoring of Thermoacoustic Combustion Instability via Recurrence Quantification Analysis and Optimized Deep Belief Network. *Symmetry* **2024**, *16*, 266. <https://doi.org/10.3390/sym16030266>

Academic Editors: Gang Yu and Shiqian Chen

Received: 18 January 2024

Revised: 13 February 2024

Accepted: 20 February 2024

Published: 22 February 2024



Copyright: © 2024 by the authors. Licensee MDPI, Basel, Switzerland. This article is an open access article distributed under the terms and conditions of the Creative Commons Attribution (CC BY) license (<https://creativecommons.org/licenses/by/4.0/>).

1. Introduction

Thermoacoustic oscillation is a phenomenon that occurs in combustion systems and is characterized by the coupling of heat release rate fluctuations and pressure fluctuations [1,2]. This intricate interaction between combustion and acoustics results in self-sustained, periodic oscillations that can significantly impact the performance and stability of combustion devices, such as gas turbines, engines, and other propulsion systems [3,4]. In thermoacoustic systems, the pressure and temperature fluctuations typically exhibit symmetric behavior in terms of their amplitude and phase. Additionally, amplitude modulation limit cycles may occur, characterized by fluctuations in amplitude, multiple frequencies, and irregular bursts [5,6]. Researchers and engineers are actively engaged in studying and mitigating thermoacoustic oscillations to enhance the performance and reliability of combustion systems. Thermoacoustic oscillations often manifest in the form of symmetric modes of vibration or oscillation. Various control methods, both passive and active, have been proposed to suppress or mitigate the impact of thermoacoustic instability [7,8].

Monitoring thermoacoustic oscillations is a crucial aspect of ensuring the stability, efficiency, and safety of combustion systems [9,10]. Several methods have been developed to detect and analyze thermoacoustic oscillations in real time [11].

Signal processing techniques, such as FFT and spectral analysis, are applied to acoustic and pressure signals to identify specific frequencies associated with thermoacoustic oscillations [12]. This helps in quantifying the characteristics of instability. However, the inherent limitation of low-frequency spectral resolution in short-time data hinders the frequency domain transformation of transient signals, such as the dynamic pressure signal at the onset of combustion oscillation, resulting in the loss of temporal details in the signal [13]. Consequently, spectrum analysis of dynamic pressure signals often proves insufficient for identifying the transition from a stable state to oscillation. Recognizing this limitation, a time-domain analysis has been proposed. As thermoacoustic instability approaches, there is a gradual increase in both the root mean squares and variances of the acoustic pressure. Song [14] suggested quantifying a combustion process using the kurtosis of dynamic pressure signals. However, owing to intermittent oscillations, beat vibrations, and other oscillation forms, these measured values do not exhibit monotonic changes. Consequently, this method is susceptible to misjudgment and lacks the ability to distinguish between various oscillation modes.

In recent years, data-driven methods utilizing machine learning tools have garnered significant attention, owing to their robust learning capabilities and adeptness in nonlinear fitting. In reference [15], a neural ordinary differential equation (neural ODE) was employed to model the entire thermoacoustic system. Zhu [16] introduced the stacked long short-term memory network (S-LSTM) for predicting future amplitudes of acoustic pressure signals. Comparative analysis against the support vector machine (SVM) revealed that S-LSTM demonstrated superior predictive performance. Ruiz [17] conducted nonlinear analysis on the sound pressure signal to generate a thresholdless recurrence plot. Moving forward, there is a clear opportunity to bridge this gap by exploring the integration of quantitative recursive graph analysis with machine learning techniques for feature extraction and classification of combustion states. Such endeavors could lead to valuable insights into the complex dynamics of combustion systems and pave the way for the development of more robust and accurate monitoring and control strategies. By leveraging these innovative approaches, researchers can advance our understanding of combustion phenomena and address critical challenges in combustion science and engineering.

This study collected data samples representing six distinct combustion states utilizing two distinct burner types—laminar and swirling. These samples encompassed a comprehensive range of combustion oscillations and were employed for the training and validation of a genetic algorithm-optimized deep belief network (GA-DBN). The study included the analysis of six types of oscillations via nonlinear analysis, with recursive quantitative analysis (RQA) being compared against three different feature extraction methods. Subsequently, multiple comparisons were conducted among GA-DBN, traditional deep belief networks (DBN), and support vector machines (SVM). Finally, the article delves into the parameter selection process during linear analysis.

2. Methods

2.1. Experimental Setup

The dataset utilized for training and validating the neural network in this article is derived from two burners illustrated in Figure 1—specifically, a laminar flow burner and a swirl burner. Each combustion chamber comprises three components: a flame burner, glass tubing, and a measurement system. In Figure 1b, the burner is depicted with a cyclone featuring 8 blades. The axial cyclone has a hub diameter of 20 mm, an outer diameter of 50 mm, and a swirl number of 0.429. The glass tube is replaceable, allowing for the replacement of various lengths of glass segments based on the experimental requirements to induce different combustion oscillation states. To ensure the sensors operate at the optimal temperature, a semi-infinite pressure tube was implemented. Acoustic pressure

data were collected using microphones (CRYSOUND type 547). A signal conditioner (PCB 482C16) was utilized to amplify the minute voltage signals, enhancing the accuracy of signal acquisition. Data were then acquired with a 16-bit analog-to-digital conversion card (NI 6212) at a sampling rate of 10 kHz. Given that the oscillation frequency of the combustion system was within 1 kHz, the digitally sampled signal faithfully preserved the information from the original signal. The fuel employed in the combustion experiment was 99.9% pure methane. The combustion state can be discerned through three methods: modifying the size of the glass tube, adjusting the relative position between the glass tube and the flame, and tuning the equivalence ratio. After analysis, we identified a total of six distinct combustion oscillation states, as illustrated in the following text.

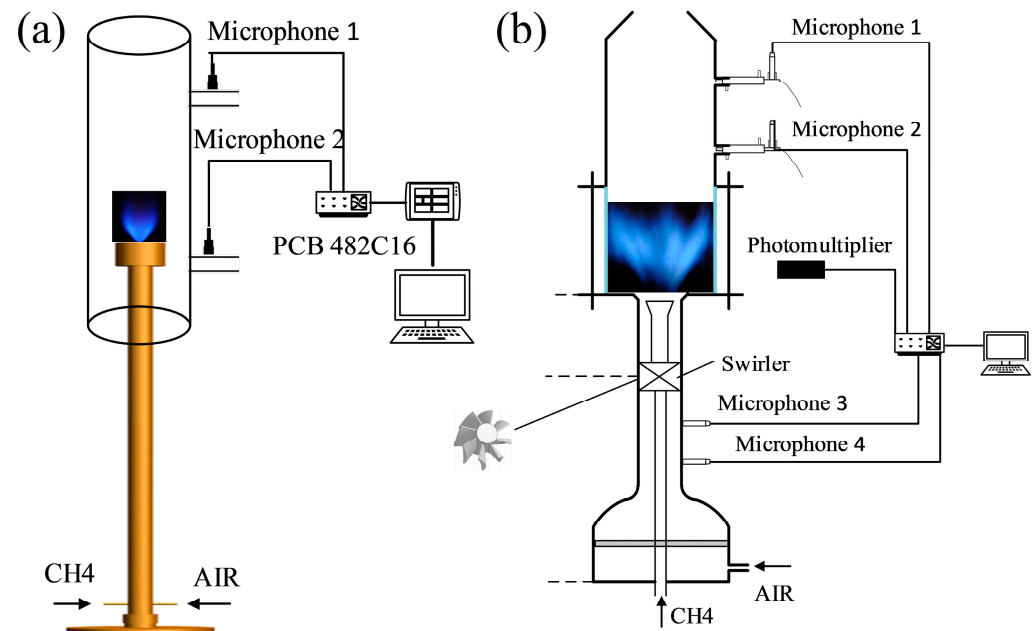


Figure 1. Schematic diagram of combustion experimental devices using (a) a Rijke tube and laminar flow burner, or (b) a swirl burner.

2.2. Nonlinear Analysis Methods

Thermoacoustic oscillations exhibit inherently nonlinear characteristics, necessitating the application of nonlinear analysis methods for a comprehensive investigation. By employing nonlinear analysis techniques, we can ascertain various types of combustion oscillations, including, but not limited to, limit cycle oscillations, intermittent oscillations, quasi-periodic oscillations, and double periodic oscillations. This article employs the method of phase space reconstruction to conduct a nonlinear analysis of sound pressure signals associated with thermoacoustic oscillations.

According to Takens' delay embedding theorem [18], given an observable time series $[x(n)]$ measured within a system, we can construct a new vector $X_i = [x(i), x(i + \tau), \dots, x(i + (m - 1)\tau)]$, where τ represents the time delay, m is the embedding dimension, and i takes values from 1 to $N - (m - 1)\tau$. Through this process, the time series is embedded into a d -dimensional phase space. The trajectory of this time series evolution is typically depicted in a phase diagram. Furthermore, the selection of the optimal delay time τ and embedding dimension m is essential. A commonly employed technique for determining the optimal time delay necessary for reconstructing the phase space is the average mutual information (AMI) method [19]. AMI assesses the correlation between $x(i)$ and $x(i + \tau)$ at a specified τ , akin to an autocorrelation function in a broader context. In this paper, the optimum τ is identified as the point corresponding to the first local minimum in the AMI. In the context of determining the optimal embedding dimension for the reconstructed phase space, the analysis has employed Cao's method [20]. Building upon the aforementioned

methodologies, the optimal delay time ($\tau = 2$ ms) and embedding dimension ($m = 10$), as illustrated in Figure 2, were chosen to embed the pressure time series into a higher-dimensional phase space.

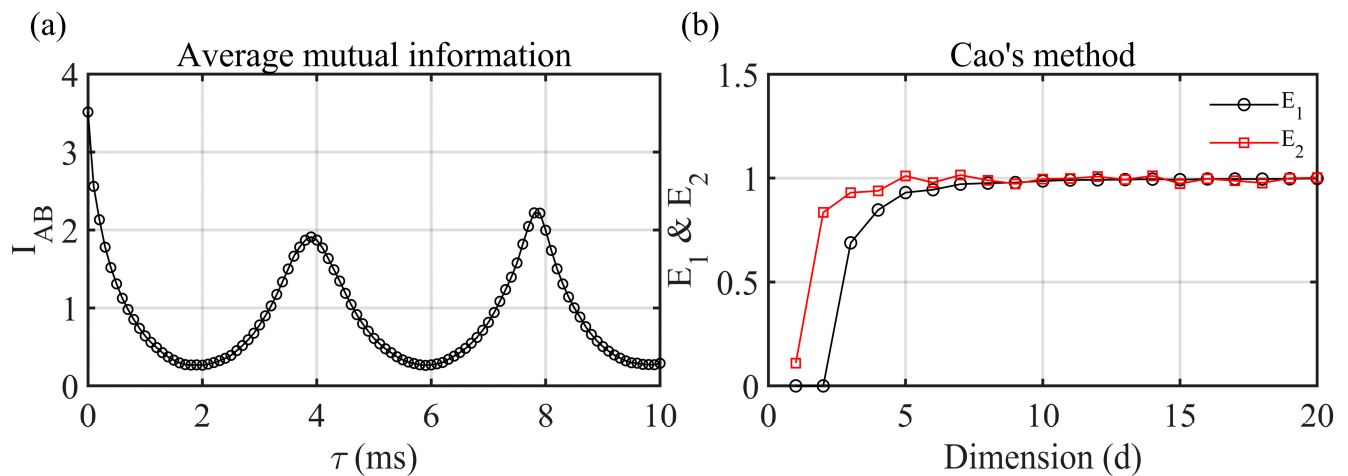


Figure 2. (a) AMI method and (b) Cao's method for phase space reconstruction.

Upon reconstructing the phase space vector, a recursive matrix can be defined as follows [21–23]:

$$R_{i,j}^{m,\varepsilon} = \Theta(\varepsilon - \|X_i - X_j\|), i, j = 1, 2, \dots, N \quad (1)$$

Here, Θ represents the Heaviside function, $\|X_i - X_j\|$ denotes the Euclidean norm representing the distance between any two points in the reconstructed phase space vector, and ε signifies the distance threshold used to determine whether two points in phase space undergo recursion. Clearly, a recursive matrix is a binary matrix composed of 0 and 1:

$$\Theta(x) = \begin{cases} 0 & x > 0 \\ 1 & x < 0 \end{cases} \quad (2)$$

Referring to Equation (2), when $\|X_i - X_j\| < \varepsilon$, $R_{i,j}^{m,\varepsilon} = 1$ signifies the occurrence of recursion between points X_i and X_j , such instances are denoted as black dots on the recursive graph. Conversely, if $\|X_i - X_j\| > \varepsilon$, $R_{i,j}^{m,\varepsilon} = 0$ indicates the absence of a recursion phenomenon, then points (i, j) on the recursion graph are represented by white dots. Additionally, Equation (2) ensures a black main diagonal in the recursive graph when calculating the distance between a point in phase space and itself. This symmetry in the recursive graph is evident as $R_{i,j}^{m,\varepsilon} = R_{j,i}^{m,\varepsilon}$. After traversing any two points in the phase space and calculating all $R_{i,j}^{m,\varepsilon}$ values, a recursive graph with a distribution of black and white points can be generated.

2.3. Deep Belief Network Optimized by Genetic Algorithm

The DBN (deep belief network) architecture is a deep neural network composed of several layers of restricted Boltzmann machines (RBMs) and one layer of backpropagation (BP) [24]. The structure of the DBN is shown in Figure 3b. RBMs consist of only two layers of neurons: visible and hidden layers. The units between the two layers are interconnected, while there are no connections within each layer. The structure of an RBM is illustrated in Figure 3a.

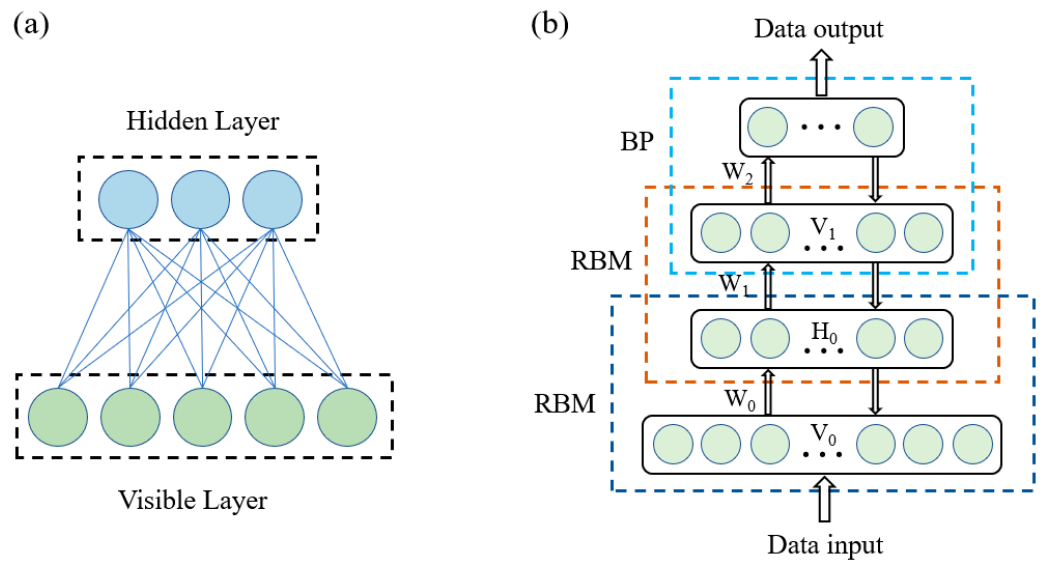


Figure 3. The schematic diagram of the basic structure of (a) an RBM and (b) a DBN.

RBM neurons are intricately connected through weights, with the visible layer denoted as V and the hidden layer as H . The extraction of meaningful features from input data is carried out by the hidden layer H , and the connection weights between the visible and hidden layers are symbolized by W . Neurons within the network exhibit binary states, being either active or inactive, denoted by 0 and 1, respectively, to signify their states. It is worth noting that RBMs operate as energy-based models. The state of the visible layer neuron i is denoted by v_i , with the corresponding bias value being a_i . Similarly, the state of hidden layer neuron j is represented by h_j and b_j signifies the corresponding bias value. The connection weight between neuron i and j is represented by w_{ij} . The RBM system's energy, contingent on the state (v, h) , can be succinctly expressed as follows:

$$E(v, h | \theta) = -\sum_{i=1}^n a_i v_i - \sum_{j=1}^m b_j h_j - \sum_{i,j=1}^{n,m} v_i w_{ij} h_j \quad (3)$$

In the formula, $\theta(w_{ij}, a_i, b_j)$ represents parameters of the RBM. Here, n and m correspond to the number of neurons in the visible and hidden layers, respectively. The joint probability distribution of (v, h) is derived from the energy function:

$$p(v, h | \theta) = \frac{1}{Z(\theta)} \exp(-E(v, h | \theta)) \quad (4)$$

Here, $Z(\theta) = \sum_{v,h} \exp(-E(v, h | \theta))$ is the normalization factor. During the training process, the normalization factor $Z(\theta)$ is typically obtained using Gibbs sampling and other sampling methods.

Since the activation states of neurons in the RBM layers are independent of each other, the j neuron in the hidden layer can be computed from the states of neurons in the visible layer. The activation probability is given by:

$$p(h_j = 1 | v, \theta) = \frac{1}{1 + \exp(-b_j - \sum_i v_i w_{ij})} \quad (5)$$

The i neuron in the visible layer is reconstructed from the hidden layer, and the activation probability is given by:

$$p(v_i = 1 | h, \theta) = \frac{1}{1 + \exp(-b_i - \sum_j h_j w_{ij})} \quad (6)$$

The maximum value of the log-likelihood function is obtained through stochastic gradient ascent, and the calculation of the change in each parameter is as follows:

$$\begin{cases} \Delta w_{ij} = \langle v_i h_j \rangle_{\text{data}} - \langle v_i h_j \rangle_{\text{recon}} \\ \Delta a_i = \langle v_i \rangle_{\text{data}} - \langle v_i \rangle_{\text{recon}} \\ \Delta b_j = \langle h_j \rangle_{\text{data}} - \langle h_j \rangle_{\text{recon}} \end{cases} \quad (7)$$

Here, $\langle * \rangle_{\text{data}}$ represents the distribution defined by the original observed data model, while $\langle * \rangle_{\text{recon}}$ represents the distribution defined by the reconstructed model.

A genetic algorithm (GA) is a computational optimization technique inspired by natural selection [25–27]. Mimicking biological evolution, GAs iteratively evolve a population of potential solutions by selecting, recombining, and mutating individuals based on their fitness. Solutions that better address a problem survive and propagate, creating diverse offspring. This process continues until an optimal or satisfactory solution is found. Leveraging a genetic algorithm for optimizing the parameters of a DBN mitigates the challenge of encountering local optima resulting from random initialization. This approach enhances the predictive performance of the DBN network. The optimization process is visually depicted in Figure 4.

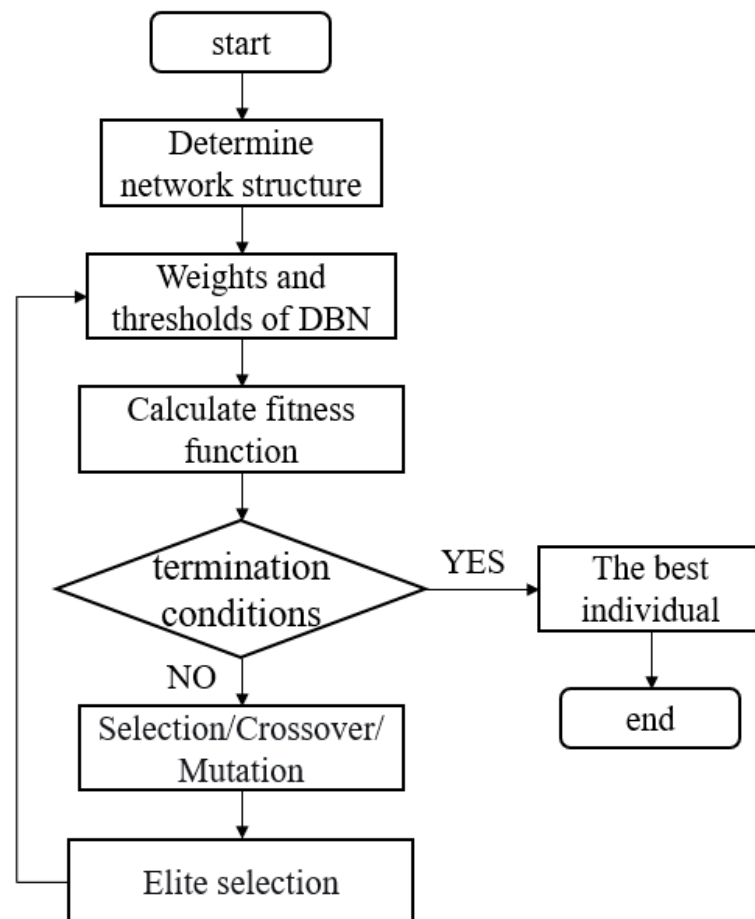


Figure 4. Process of genetic algorithm for parameter optimization of a DBN network.

3. Results and Discussion

3.1. Recurrence Plot Analysis of Combustion States

Through the manipulation of the burner's operating conditions, we achieved a set of six diverse combustion oscillation states, denoted as Case 1 to Case 6. These states are visualized in Figures 5 and 6.

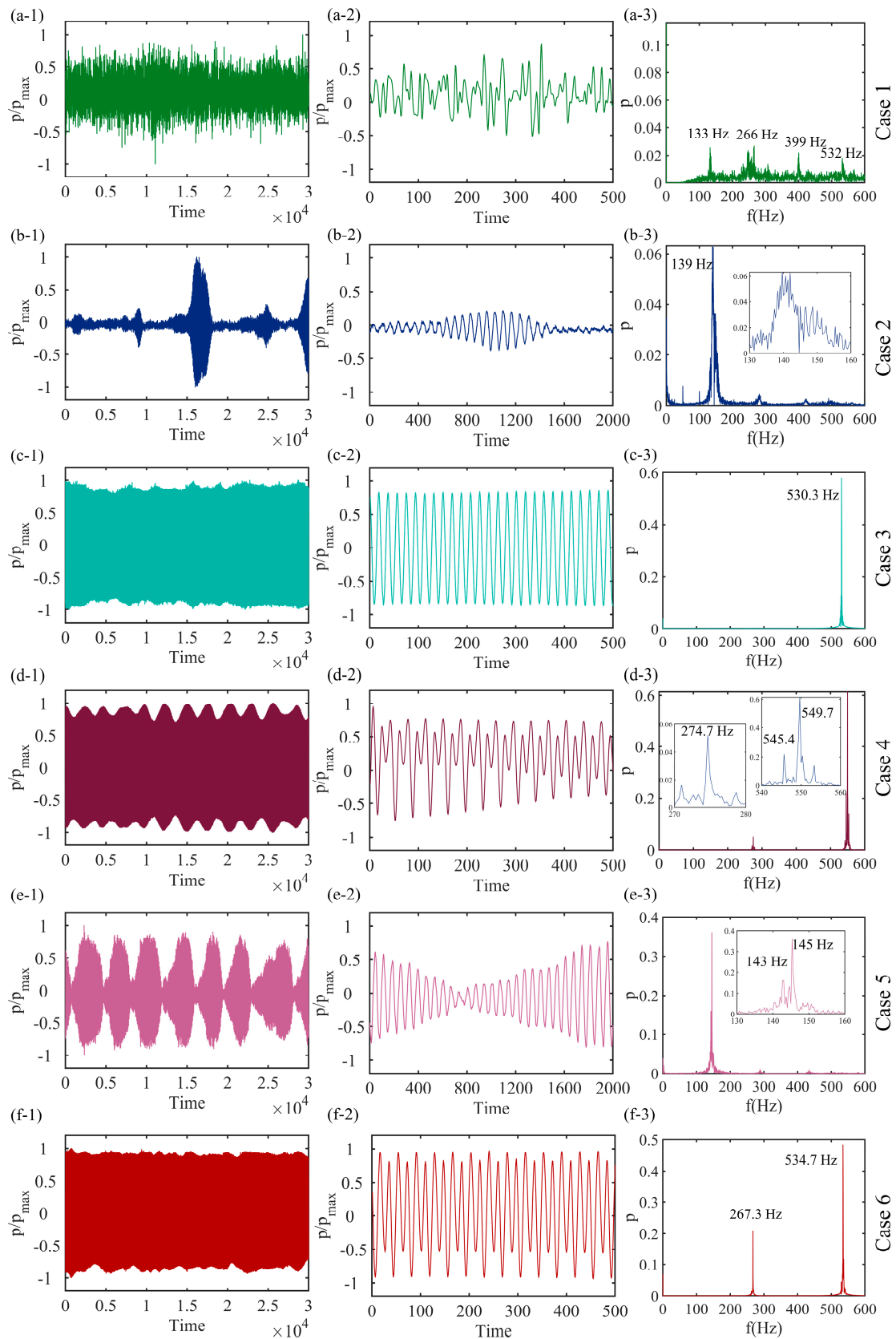


Figure 5. Time and frequency domain diagrams of six combustion oscillation states: (a-1–f-1) show the time-domain plots, (a-2–f-2) show the local details of the time-domain plots, and (a-3–f-3) show the frequency-domain plots.

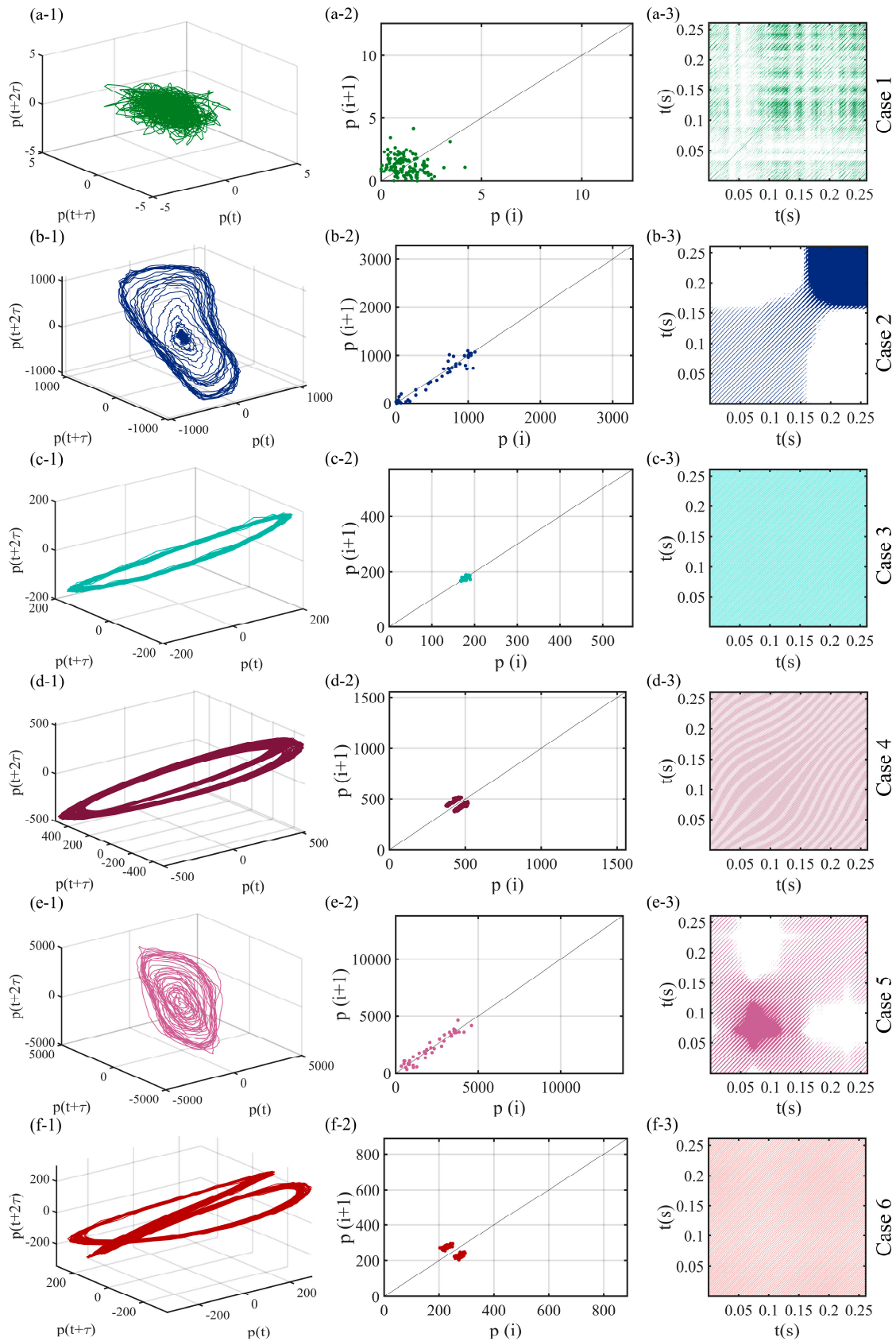


Figure 6. A nonlinear analysis of six distinct combustion oscillation states: (a-1–f-1) illustrate the 3D phase plots, (a-2–f-2) showcase the Poincaré sections, and (a-3–f-3) display the recurrence plots.

Figure 5 presents a comprehensive overview of the time-domain and frequency-domain characteristics associated with six distinct combustion oscillation states. Specifically, Figure 5(a-1-f-1) provide the primary time-domain graphs, offering a broad perspective. Figure 5(a-2-f-2) zoom in on local details within the time-domain graphs, providing a closer examination of specific features. Meanwhile, Figure 5(a-3-f-3) display the corresponding frequency-domain graphs, capturing the oscillatory patterns and frequencies associated with each combustion state. In Case 1, a stable state is observed, where the time-domain graph is predominantly characterized by environmental noise, lacking regularity. Although a peak of 133 Hz and its harmonic frequency is discernible in the frequency domain diagram, the amplitude of this peak is notably small. Moving on to Case 2, intermittent peaks emerge in the time-domain plot, displaying different amplitudes. Oscillating pulses randomly manifest in the non-periodic signals, and Figure 5(b-2) reveals a discernible pattern in the appearance of these pulses. The frequency domain diagram depicts a clear peak at 139 Hz with a relatively wide bandwidth. This type of oscillation is commonly referred to in the literature as intermittent oscillation. Case 3 distinctly exhibits a limit cycle oscillation, characterized by a regular sine time series in pressure oscillation. The frequency domain diagram highlights the presence of a single dominant frequency at 530.3 Hz. In Case 4, the frequencies of the first and second modes are identified as 274.7 Hz and 549.7 Hz, respectively, and they are not integer multiples. When these two modes are simultaneously excited, a frequency difference phenomenon occurs, leading to variation in the amplitude of the waveform in the time-domain graph over time. The principle of modal superposition provides a better explanation for this phenomenon. Case 5 aligns with the literature's description of beat vibration. The time-domain diagram illustrates low-frequency periodic changes in the amplitude of the oscillation. Multiple adjacent peaks near the main frequency in the frequency spectrum of the beat vibration suggest the result of linear superposition of vibrations with similar frequencies. Finally, Case 6 displays two amplitudes in the time-domain plot, with peaks at 534.7 Hz and 267.3 Hz in the frequency domain diagram. This characteristic pattern is indicative of a typical period-2 oscillation. In summary, the detailed analysis of each combustion oscillation state provides valuable insights into their distinct behaviors and underlying dynamics, as depicted in the time- and frequency-domain diagrams.

Given the nonlinear nature of thermoacoustic oscillations, the complete representation of the system's inherent dynamic characteristics goes beyond the capabilities of time-domain and frequency-domain diagrams alone. Figure 6 presents a nonlinear analysis of six distinct combustion oscillation states. In particular, Figure 6(a-1-f-1) illustrate the 3D phase plots, Figure 6(a-2-f-2) showcase the Poincaré sections, and Figure 6(a-3-f-3) display the recurrence plots. In Case 1, characterized by a stable state, the trajectories on the strange attractor exhibit random movement in the phase space, indicating an inability to follow a periodic orbit. The Poincaré profile displays scattered points, and the recursive graph depicts the presence of vertical and horizontal lines, signaling slow or unchanged states, with evenly distributed points, suggesting white noise. Case 2 manifests as an intermittent oscillation state, as depicted by a 3D phase plot featuring two dense, concentric disks—an outer and an inner disk. During bursts, trajectories are propelled to the outer disk and subsequently reintroduced to the inner region, mirroring the characteristic behavior observed in intermittent oscillations across various nonlinear systems, known as intermittency. The Poincaré section exhibits a diagonal distribution of numerous points, and the recurrence plot unveils intricate details about the system's transition to bursts, embedded within a kite-like structure. Tracing the main diagonal in the recurrence plot essentially tracks the temporal evolution of the system. Preceding a burst, the system dynamics are characterized by limit cycle oscillations. Over time, the limit cycle undergoes a gradual transformation toward quasi-periodic behavior. In the moments just preceding a burst, the recurrence plot notably highlights the emergence of quasi-periodic dynamics. In Case 3, the limit cycle state is identified by a distinct closed-loop phase plot, a relatively concentrated point in the Poincaré cross-section, and

periodic repetitive structures in recursive graphs, such as equidistant diagonals. Case 4 represents a differential frequency oscillation state, with the phase diagram displaying orbits forming two loops. The Poincaré cross-section shows two relatively concentrated points on either side of the diagonal, and the recursive graph exhibits a wavy pattern. Moving to Case 5, the beat vibration state, the three-dimensional phase diagram forms a concentric disk with a relatively uniform orbit distribution. The Poincaré cross-section features many points distributed along the diagonal, showing a more uniform distribution compared to intermittent oscillations. The recursive diagram resembles a kite-like structure, capturing the process of beat oscillation from periodic to burst. Finally, Case 6, a period-2 oscillation state, is characterized by a phase diagram displaying orbits forming two loops, indicating a doubling of the oscillation period compared to limit cycle oscillation. The Poincaré cross-section reveals two concentrated points, and a clear separation diagonal is evident in the recursive graph. This detailed analysis provides valuable insights into the diverse dynamic behaviors exhibited by each combustion oscillation state.

Based on the aforementioned analysis, it can be deduced that nonlinear analysis of combustion systems is capable of discerning various combustion states. Nevertheless, there is a perceived inefficiency in recognition. It is proposed that summarizing linear analysis into several quantitative indicators may enhance clarity and efficiency in identifying combustion states.

3.2. Quantitative Feature Extraction Based on Recurrence Plots

While recursive graphs offer an intuitive representation of a system’s dynamic characteristics through two-dimensional images, there exists a need for quantitative methods to describe its motion state. Marwan [21–23] introduced a methodology involving the calculation of recursive points, diagonals, and other microscopic texture structures within recursive graphs. This approach allows for the quantification of the recursive phenomenon in the system, enabling the expression of the system’s dynamic characteristics in numerical form. Table 1 enumerates the quantification methods employed in this article.

Table 1. Quantitative approaches in recursive quantitative analysis.

Parameters	Expression	Parameters	Expression
RR	$\frac{1}{N^2} \sum_{i,j=1}^N R_{i,j}^{m,\epsilon}$	P_{max}	$max\{P_i, i = 1, \dots, N_v\}$
DET	$\frac{\sum_{l=l_{min}}^N IP(l)}{\sum_{i,j=1}^N R_{i,j}^{m,\epsilon}}$	T_j^1	$\left\{ i, j : X_i, X_j \in R_i \right\}$
L_{ave}	$\frac{\sum_{l=l_{min}}^N IP(l)}{\sum_{l=l_{min}}^N P(l)}$	T_j^2	$\left\{ i, j : X_i, X_j \in R_i; X_{j-1} \notin R_i \right\}$
L_{max}	$max\{L_i, i = 1, \dots, N_l\}$	RPDE	$-\frac{\sum_{t=1}^{T_{max}} P(t) \ln P(t)}{\ln(T_{max})}$
ENTR	$-\sum_{l=l_{min}}^N P(l) \ln P(l)$	C_1	$\frac{N}{\sum_{i=1}^N \sum_{j,k=1}^N R_{i,j}^{m,\epsilon} R_{j,k}^{m,\epsilon} R_{k,i}^{m,\epsilon}}$
LAM	$\frac{\sum_{v=v_{min}}^N vP(v)}{\sum_{i,j=1}^N R_{i,j}^{m,\epsilon}}$	C_2	$\frac{\sum_{i,j,k=1}^N R_{i,j}^{m,\epsilon} R_{j,k}^{m,\epsilon} R_{k,i}^{m,\epsilon}}{\sum_{i,j,k=1}^N R_{i,j}^{m,\epsilon} R_{k,i}^{m,\epsilon}}$
TT	$\frac{\sum_{v=v_{min}}^N v \cdot P(v)}{\sum_{v=v_{min}}^N P(v)}$		

Recursion rate (RR) is defined as the percentage of recursion points within a recursive graph relative to the total number of points. Determinism (DET) is characterized as the percentage of the total number of recursive points located in line segments parallel to the main diagonal within a recursive graph. Here, $P(l)$ represents the probability distribution of the length l of the parallel diagonal in the recursive graph, with l_{min} denoting the minimum diagonal length. The length of each parallel diagonal (l) is calculated. This calculation typically involves measuring the distance along the diagonal line formed by the connected nodes. This distance can be calculated using various metrics, such as the Euclidean distance between nodes in phase space, which is adopted in this paper. Entropy

of diagonal length (ENTR) refers to the Shannon entropy [28] calculated from the frequency distribution of diagonal lines of varying lengths within a recursive graph. Laminarity (LAM) is determined as the percentage of vertical lines within the recurrence plot relative to the total number of recursive points. Here, $P(v)$ represents the probability distribution of a vertical line with a length of v in a recursive graph. Additional characteristic parameters include average diagonal length (L_{ave}), length of longest diagonal line (L_{max}), trapping time (TT), length of longest vertical line (P_{max}), recurrence times of first type (T_j^1), recurrence times of second type (T_j^2), recurrence period density entropy (RPDE), clustering coefficient (C_1), and transitivity (C_2).

Diverse quantization parameters capture various details of oscillation states within recursive graphs from distinct perspectives. Figure 7 elucidates the quantification outcomes derived from three quantitative methods—RR, TT, and RPDE—in diverse oscillation states. In Case 1, representing a stable combustion state, both RR and TT values maintain a proximity to -1 , with subtle fluctuations over time. Meanwhile, RPDE values exhibit significant variation within the range of -1 to 1 , lacking a discernible pattern. Shifting to Case 2, emblematic of an intermittent oscillation state, the transition between stable combustion and oscillation states induces noticeable changes in RR. It increases from -1 in the stable state to approximately 0.5 during oscillation, with fluctuating values around 0.5 due to irregular oscillations. TT values follow a similar trend to RR, stabilizing around 0 during oscillation, while RPDE values become more regular, converging toward stability. In Case 3, representing a limit cycle oscillation state, RR, TT, and RPDE converge to a stable value, reflecting the strong periodicity evident in the sound pressure time series during limit cycle oscillation. Case 4, portraying differential frequency oscillation, witnesses stable RR, TT, and RPDE values closely correlated with the amplitude of the sound pressure time series. Case 5, characterized by beat oscillation, exhibits large variations in amplitude over time, resulting in substantial fluctuations in RR, TT, and RPDE values. Lastly, in Case 6, representing period-2 oscillation, the TT value maintains relative constancy, while RR and RPDE values display systematic variations in correspondence with the amplitude of the sound pressure time series. In summary, the comprehensive analysis of RR, TT, and RPDE as quantification parameters underscores their efficacy in effectively distinguishing between different oscillation states.

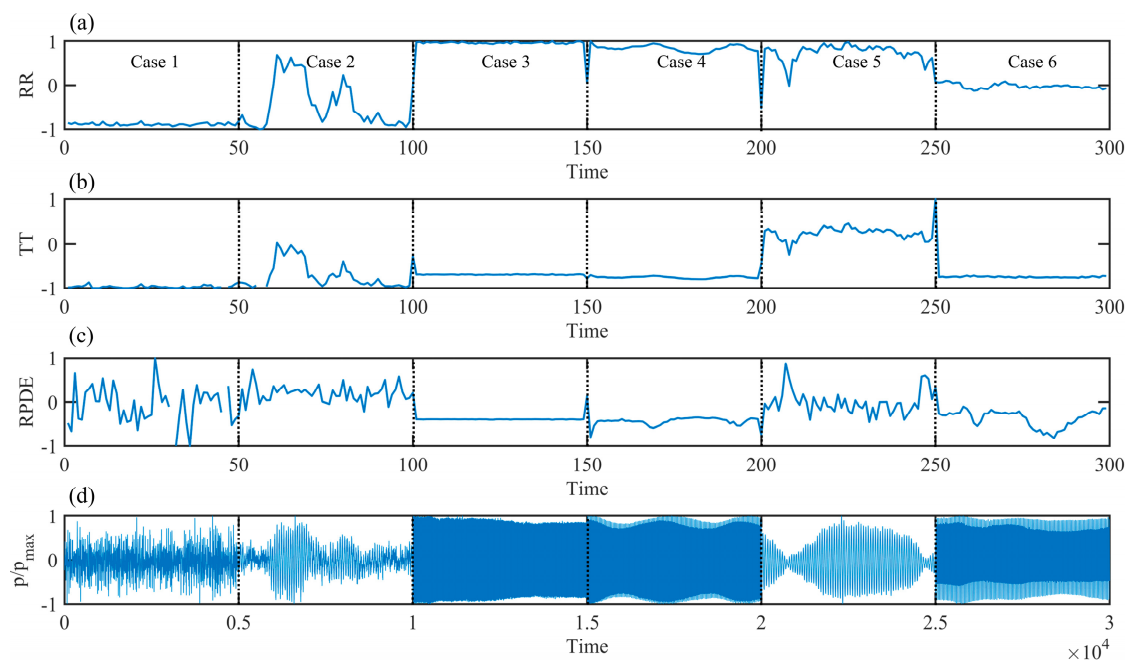


Figure 7. Comparing various quantitative characteristic parameters across different oscillation states: (a) RR, (b) TT, (c) RPDE, and (d) different oscillation states.

3.3. Monitoring Performance Based on Optimized Deep Belief Network

3.3.1. Evaluation of GA-DBN Prediction Outcomes

Thirteen feature parameters, representing distinct combustion states, were derived through the quantification of recursive graphs. Due to the impracticality of manually and swiftly analyzing and determining combustion states based on these feature parameters, we opted for the GA-DBN method to efficiently classify combustion states.

Figure 8 illustrates the classification outcomes of GA-DBN, with Figure 8a showcasing the classification results for 3486 sample data. Figure 8b presents the confusion matrix associated with these classification results. Examining Figure 8a, it is evident that only six data samples were misclassified, yielding a remarkable prediction accuracy of 99.83% for this experiment. Figure 8b offers an in-depth analysis of the classification scenario using the confusion matrix. All 581 samples in Case 1 were accurately predicted, with no instances of other combustion states being erroneously classified as Case 1. For Case 2, out of 581 samples, 580 were correctly predicted, and only 1 sample was inaccurately classified as Case 5. Further analysis suggests that Case 2 exhibits intermittent oscillation, characterized by significant amplitude variations over time, resembling the beating feature of Case 5. When the time window of the time series is short, it might fail to capture the complete characteristics of intermittent oscillation, leading to misclassification as beating oscillation. One sample in Case 4 was misclassified as Case 3, with no other combustion states being erroneously classified as Case 4. In Case 3, out of 581 samples, 580 were correctly predicted, while 1 sample was mistakenly classified as Case 6. This misclassification can be attributed to the relatively similar features of these two combustion states. For Case 5, 579 out of 581 samples were accurately predicted, with 1 sample each being misclassified as Case 6 and Case 4. In Case 6, 580 out of 581 samples were correctly predicted, with 1 sample mistakenly classified as Case 4. In summary, it was observed that Case 3, Case 4, and Case 6 are more susceptible to misclassification due to their regular oscillatory nature.

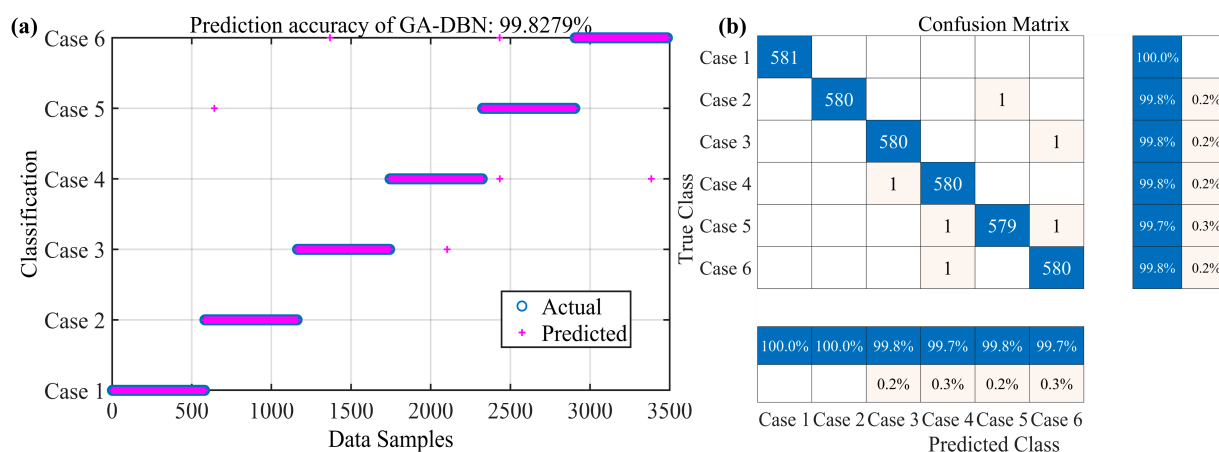


Figure 8. The classification results of GA-DBN: (a) represents the classification results and (b) depicts the confusion matrix of the classification results.

3.3.2. Comparative Analysis of Diverse Feature Extraction and Classification Methods

In this section, we present a comprehensive examination of various feature extraction and classification methods employed for monitoring thermoacoustic combustion instability. The aim was to assess the efficacy of different algorithms in capturing and classifying critical combustion instability patterns.

As shown in Figure 9, Figure 9a displays the comparative results of feature extraction algorithms. Figure 9a illustrates the performance of three distinct feature extraction algorithms: recursive quantification analysis (RQA): This method relies on recursive graph analysis to derive thirteen feature parameters representing different combustion states. Energy entropy of empirical mode decomposition (EMD): This approach leverages the

energy entropy derived from EMD to capture intricate details of combustion instability dynamics. Time-domain and frequency-domain features (TF): Traditional time-domain and frequency-domain features are extracted to provide a baseline for comparison. In Figure 9a, the accuracy of the RQA method remains consistently near 100%, significantly outperforming the other two methods. This robust and reliable performance showcases the effectiveness of the RQA algorithm in accurately extracting features related to thermoacoustic combustion instability, making it a standout performer in comparison to the other two methods. The EMD method performs relatively well, while the TF method shows the lowest performance. The time-domain and frequency-domain features (TF) method lags behind, indicating limitations in accurately representing the intricate patterns inherent in thermoacoustic combustion instability. Additionally, across eight experiments, both the EMD and TF methods exhibited significant fluctuations in prediction accuracy, whereas the RQA method consistently achieved desirable prediction results in each trial.

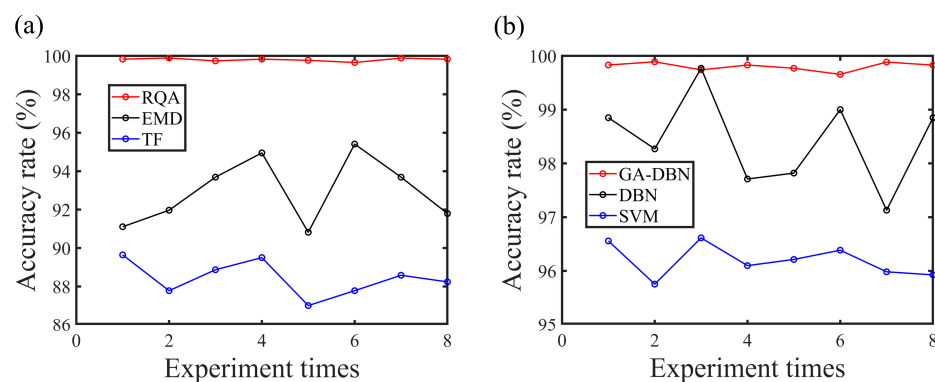


Figure 9. Comparative analysis of results using various methods: (a) different feature extraction methods; (b) different classification algorithms.

Moving beyond feature extraction, Figure 9b delves into the comparison of three classification algorithms: genetic algorithm-optimized deep belief network (GA-DBN): This method combines the power of genetic algorithms with deep belief networks for efficient and accurate classification of combustion states. Deep belief network (DBN): A standard deep belief network is employed to evaluate its performance in comparison to the optimized GA-DBN. Support vector machine (SVM): As a widely used classification algorithm, SVM serves as a benchmark for assessing the effectiveness of deep learning approaches. The results depicted in Figure 9b reveal that the genetic algorithm-optimized deep belief network (GA-DBN) method consistently achieves exceptional accuracy, with its performance maintaining stability around the 100% mark. This indicates the effectiveness of the genetic algorithm in optimizing the parameters of the deep belief network, resulting in a highly accurate and stable classification of combustion states. The DBN method takes the second place, and the SVM method has the worst performance. The random initialization of parameters in the DBN method can result in different starting points for the optimization process, leading to variations in the final accuracy achieved. This highlights a potential limitation in the DBN method, emphasizing the significance of optimizing the initialization process for achieving more consistent and reliable results.

3.3.3. The Influence of Various Recursive Analysis Parameters on Outcome

The analysis of thermoacoustic combustion instability reveals that the parameters governing linear analysis—specifically, the length of the time series and the step size (L) of the time window movement—significantly influence prediction outcomes. By systematically varying these parameters, with the selection of five window lengths ranging from 200 to 2000 and three step sizes ($L = 50$, $L = 100$, and $L = 200$), the experiment in Figure 10 exposes crucial trends. Notably, an increase in window length correlates positively with enhanced prediction accuracy, as longer windows capture finer details of combustion instability

dynamics. However, this improvement comes at the expense of longer computation times. It is vital to strike a balance, as excessively long windows, while yielding higher accuracy, may introduce challenges in practical applications, potentially leading to errors during state transitions. Additionally, the experiment highlights that larger step sizes result in diminished prediction accuracy, emphasizing the trade-off between capturing crucial information and maintaining high prediction precision. Achieving an optimal configuration of these parameters is essential for the effective real-world application of thermoacoustic combustion instability monitoring.

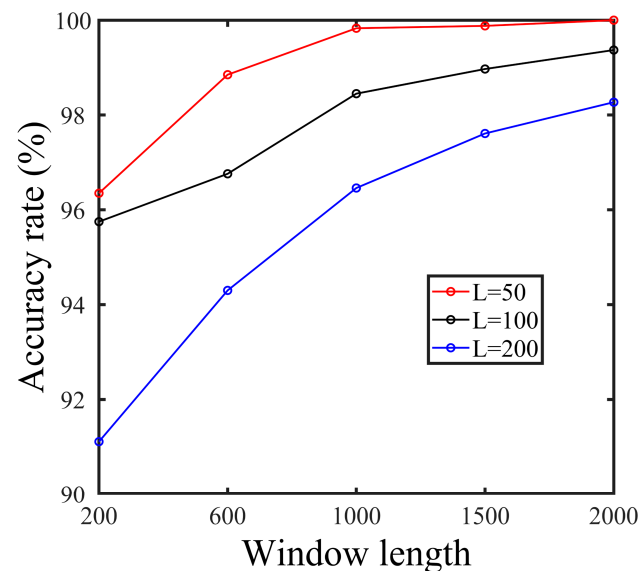


Figure 10. The influence of different window lengths and step sizes on prediction results.

4. Conclusions

In conclusion, this paper has presented a comprehensive exploration into the monitoring of thermoacoustic combustion instability through the innovative integration of recursive quantitative analysis (RQA) and GA-DBN. Our study included a meticulous comparison of three different feature extraction methods, revealing that recursive quantitative analysis (RQA) emerged as the standout performer in capturing the intricate features associated with combustion states. This underscores the significance of leveraging RQA for its outstanding performance in enhancing the accuracy and reliability of combustion state monitoring. Furthermore, we conducted extensive multiple comparisons between GA-DBN, conventional deep belief networks (DBN), and support vector machines (SVM). The results of these comparisons unequivocally demonstrate the superior classification capabilities of GA-DBN, with the model achieving not only impressive but also satisfactory classification results across various combustion states. This reinforces the effectiveness of the genetic algorithm optimization in enhancing the performance of deep belief networks for thermoacoustic combustion instability monitoring. The insights gained from this study not only deepen our understanding of thermoacoustic combustion instability but also provide a robust framework for addressing the challenges associated with classification tasks in diverse combustion processes. We will use this method to monitor the combustion status in real time, providing reference for adjusting the combustion status of gas turbines.

Author Contributions: Methodology, Q.Z. and J.S.; investigation, Q.Z., Y.S. and K.M.; writing—original draft preparation, Q.Z., C.H. and K.M.; writing—review and editing, Q.Z., J.S., Y.S. and K.M.; visualization, Q.Z.; supervision, C.H.; project administration, C.H.; funding acquisition, C.H. All authors have read and agreed to the published version of the manuscript.

Funding: This research was funded by the National Science and Technology Major Project, grant number J2019-III-0020-0064.

Data Availability Statement: Data are contained within the article.

Conflicts of Interest: The authors declare no conflicts of interest.

References

1. Zhao, D.; Gutmark, E.; de Goeij, P. A review of cavity-based trapped vortex, ultra-compact, high-g, inter-turbine combustors. *Prog. Energy Combust. Sci.* **2018**, *66*, 42–82. [[CrossRef](#)]
2. Zhao, D.; Lu, Z.; Zhao, H.; Li, X.; Wang, B.; Liu, P. A review of active control approaches in stabilizing combustion systems in aerospace industry. *Prog. Aerosp. Sci.* **2018**, *97*, 35–60. [[CrossRef](#)]
3. Webster, S.; Hardi, J.; Oswald, M. Measurement of acoustic dissipation in an experimental combustor under representative conditions. *J. Sound Vib.* **2017**, *390*, 39–54. [[CrossRef](#)]
4. Poinso, T. Prediction and control of combustion instabilities in real engines. *Proc. Combust. Inst.* **2017**, *36*, 1–28. [[CrossRef](#)]
5. Juniper, M.P.; Sujith, R. Sensitivity and Nonlinearity of Thermoacoustic Oscillations. *Annu. Rev. Fluid Mech.* **2018**, *50*, 661–689. [[CrossRef](#)]
6. Boudy, F.; Durox, D.; Schuller, T.; Candel, S. Nonlinear flame describing function analysis of galloping limit cycles featuring chaotic states in premixed combustors. In Proceedings of the ASME Turbo Expo 2012: Turbine Technical Conference and Exposition, Copenhagen, Denmark, 11–15 June 2012; pp. 713–724.
7. Zhao, D.; Li, X. A review of acoustic dampers applied to combustion chambers in aerospace industry. *Prog. Aerosp. Sci.* **2015**, *74*, 114–130. [[CrossRef](#)]
8. Zhao, D.; Reyhanoglu, M. Feedback control of acoustic disturbance transient growth in triggering thermoacoustic instability. *J. Sound Vib.* **2014**, *333*, 3639–3656. [[CrossRef](#)]
9. Li, Y.; Hu, C.; Zhao, Q.; Yang, J.; Tan, X.; Xu, G. Experimental Investigation of Flame Dynamics Based on High-Speed Images in Swirl Combustion Systems. *J. Therm. Sci.* **2022**, *32*, 427–437. [[CrossRef](#)]
10. Li, Y.; Hu, C.; Shen, Y.; Han, B.; Yang, J.; Xu, G. A New Methodology for Early Detection of Thermoacoustic Combustion Oscillations Based on Permutation Entropy. *J. Therm. Sci.* **2023**, *32*, 2310–2320. [[CrossRef](#)]
11. Zeng, Q.; Hu, C.; Xu, H.; Sun, J.; Tan, X.; Zhu, J. Prediction of acoustic pressure of thermoacoustic combustion instability based on Elman neural network. *J. Low Freq. Noise Vib. Act. Control* **2023**, *42*, 1519–1530. [[CrossRef](#)]
12. Joo, S.; Choi, J.; Kim, N.; Lee, M.C. A novel diagnostic method based on filter bank theory for fast and accurate detection of thermoacoustic instability. *Sci. Rep.* **2021**, *11*, 3043. [[CrossRef](#)]
13. Waxenegger-Wilfing, G.; Sengupta, U.; Martin, J.; Armbruster, W.; Hardi, J.; Juniper, M.; Oswald, M. Early detection of thermoacoustic instabilities in a cryogenic rocket thrust chamber using combustion noise features and machine learning. *Chaos Interdiscip. J. Nonlinear Sci.* **2021**, *31*, 63128. [[CrossRef](#)] [[PubMed](#)]
14. Song, W.J.; Cha, D.J. Temporal kurtosis of dynamic pressure signal as a quantitative measure of combustion instability. *Appl. Therm. Eng.* **2016**, *104*, 577–586. [[CrossRef](#)]
15. Dhadphale, J.M.; Unni, V.R.; Saha, A.; Sujith, R.I. Neural ODE to model and prognose thermoacoustic instability. *Chaos* **2022**, *32*, 13131. [[CrossRef](#)] [[PubMed](#)]
16. Lyu, Z.; Fang, Y.; Zhu, Z.; Jia, X.; Gao, X.; Wang, G. Prediction of acoustic pressure of the annular combustor using stacked long short-term memory network. *Phys. Fluids* **2022**, *34*, 54109. [[CrossRef](#)]
17. Ruiz, E.A.; Unni, V.R.; Pavithran, I.; Sujith, R.I.; Saha, A. Convolutional neural networks to predict the onset of oscillatory instabilities in turbulent systems. *Chaos Interdiscip. J. Nonlinear Sci.* **2021**, *31*, 93131. [[CrossRef](#)] [[PubMed](#)]
18. Packard, N.H.; Crutchfield, J.P.; Farmer, J.D.; Shaw, R.S. Geometry from a Time Series. *Phys. Rev. Lett.* **1980**, *45*, 712–716. [[CrossRef](#)]
19. Fraser, A.M.; Swinney, H.L. Independent coordinates for strange attractors from mutual information. *Phys. Rev. A* **1986**, *33*, 1134–1140. [[CrossRef](#)] [[PubMed](#)]
20. Cao, L. Practical method for determining the minimum embedding dimension of a scalar time series. *Phys. D Nonlinear Phenom.* **1997**, *110*, 43–50. [[CrossRef](#)]
21. Kraemer, K.H.; Marwan, N. Border effect corrections for diagonal line based recurrence quantification analysis measures. *Phys. Lett. A* **2019**, *383*, 125977. [[CrossRef](#)]
22. Marwan, N. How to avoid potential pitfalls in recurrence plot based data analysis. *Int. J. Bifurc. Chaos* **2011**, *21*, 1003–1017. [[CrossRef](#)]
23. Marwan, N.; Donges, J.F.; Zou, Y.; Donner, R.V.; Kurths, J. Complex network approach for recurrence analysis of time series. *Phys. Lett. A* **2009**, *373*, 4246–4254. [[CrossRef](#)]
24. Hinton, G.E.; Osindero, S.; Teh, Y.-W. A Fast Learning Algorithm for Deep Belief Nets. *Neural Comput.* **2006**, *18*, 1527–1554. [[CrossRef](#)] [[PubMed](#)]
25. Xie, Y.; Gui, F.-X.; Wang, W.-J.; Chien, C.-F. A Two-stage Multi-population Genetic Algorithm with Heuristics for Workflow Scheduling in Heterogeneous Distributed Computing Environments. *IEEE Trans. Cloud Comput.* **2021**, *11*, 1446–1460. [[CrossRef](#)]
26. Chen, R.; Yang, B.; Li, S.; Wang, S. A self-learning genetic algorithm based on reinforcement learning for flexible job-shop scheduling problem. *Comput. Ind. Eng.* **2020**, *149*, 106778. [[CrossRef](#)]

-
27. Katoch, S.; Chauhan, S.S.; Kumar, V. A review on genetic algorithm: Past, present, and future. *Multimed. Tools Appl.* **2021**, *80*, 8091–8126. [[CrossRef](#)]
 28. Lin, J. Divergence measures based on the Shannon entropy. *IEEE Trans. Inform. Theory* **1991**, *37*, 145–151. [[CrossRef](#)]

Disclaimer/Publisher’s Note: The statements, opinions and data contained in all publications are solely those of the individual author(s) and contributor(s) and not of MDPI and/or the editor(s). MDPI and/or the editor(s) disclaim responsibility for any injury to people or property resulting from any ideas, methods, instructions or products referred to in the content.